Short communication

Layer-dependent supercapacitance of graphene films grown by chemical vapor deposition on nickel foam

Wei Chen, Zhongli Fan, Gaofeng Zeng, Zhiping Lai*

Advanced Membranes and Porous Materials Center, Division of Physical Science and Engineering, King Abdullah University of Science and Technology (KAUST), Thuwal 23955-6900, Saudi Arabia

HIGHLIGHTS

► High quality, large-area graphene films are synthesized on Ni foam using chemical vapor deposition.
► The number of graphene layers is adjusted by varying the rate of the cooling process.
► The capacitive properties of graphene films are related to the number of graphene layers.
► The specific capacitance of thinner graphene films is almost twice that of thicker ones and is stable up to 1000 cycles.

GRAPHICAL ABSTRACT
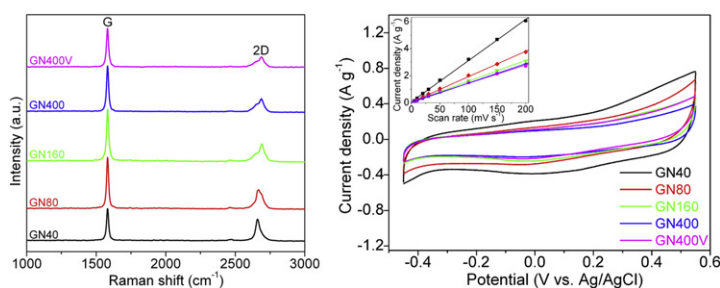
ARTICLE INFO

ABSTRACT

High-quality, large-area graphene films with few layers are synthesized on commercial nickel foams under optimal chemical vapor deposition conditions. The number of graphene layers is adjusted by varying the rate of the cooling process. It is found that the capacitive properties of graphene films are related to the number of graphene layers. Owing to the close attachment of graphene films on the nickel substrate and the low charge-transfer resistance, the specific capacitance of thinner graphene films is almost twice that of the thicker ones and remains stable up to 1000 cycles. These results illustrate the potential for developing high-performance graphene-based electrical energy storage devices.

© 2012 Elsevier B.V. All rights reserved.

1. Introduction

Graphene, a two-dimensional hexagonal lattice of sp^2-hybridized carbon atoms, has attracted considerable attention because of its exceptional properties, such as large surface area, extraordinary elasticity, high thermal and electric conductivity, and high mobility of charge carriers [1–3]. Promising advances in catalysis, energy storage and electronic device fields can be made by utilizing the fascinating properties of graphene [4–6]. To realize this potential, large-scale, reliable and controllable production for high-quality graphene is required. In comparison with other methods, chemical vapor deposition (CVD) can produce single- to few-layer, high-quality, large-area graphene films with low cost and high efficiency, thus showing a promising prospect for the controlled and scalable production of graphene [7–9]. Graphene and its derivatives recently emerged as alternative electrode materials of

---

* Corresponding author. Tel.: +966 2 8082408; fax: +966 2 8021282.
E-mail address: zhiping.lai@kaust.edu.sa (Z. Lai).

supercapacitors and attracted increasing interests [10–12]. Stoller et al. reported that chemically modified graphene exhibited large capacitance of 135 F g^{-1} in aqueous electrolyte [10]. Miller et al. demonstrated that vertical graphene grown on nickel foam showed excellent frequency response as double-layer capacitor [11]. Graphene materials prepared from graphene oxide using gas-based hydrazine by Wang et al. showed the specific capacitance as high as 205 F g^{-1} [12]. It has been previously established that the number of layers plays an important role in customizing graphene properties [13,14]. However, the effect of the layer number and surface wrinkles of graphene on the supercapacitance has not yet been explored. In this work, we synthesized high-quality, large-area graphene films with various thicknesses onto Ni foams under optimized CVD conditions [15]. Cooling rate and vacuum were used to obtain different numbers of layers by adjusting the segregation of carbon species at high temperature. The layer-dependent capacitive behaviors of graphene were then investigated.

2. Experimental section

2.1. Synthesis of graphene films

Commercial Ni foam (Lyrun Co., purity >99.9%, 90 PPI) was purged with methanol, isopropanol, and deionized water in turn and then dried at 100 °C in a N$_2$ atmosphere. After evacuation of the CVD chamber (quartz tube), the clean Ni foam piece (with size 2 × 2 cm, surface area about 800 cm^2, mass about 160 mg) was heated to 1000 °C in the forming gas (H$_2$/Ar, 200/500 ml min^{-1}) and was kept at this temperature for 15 min to reduce the surface oxide layer. After reduction, the Ni foam was exposed to methane (10 ml min^{-1}, in H$_2$/Ar, 200/500 ml min^{-1}) at 1000 °C for 5 min and then cooled in H$_2$/Ar (200/500 ml min^{-1}). The cooling rates were controlled by opening the furnace cover and changing the position of the samples. This was performed in 2–3 s, and the cooling rates were monitored by a thermal couple fixed at the sample holder. Different cooling rates, corresponding to 40 (±3), 80 (±7), 160 (±12), 400 (±20) °C min^{-1} were employed. The general process of preparing graphene films is summarized in Scheme 1. The resulting samples were denoted as GN40, GN80, GN160, GN400, respectively. The sample that cooled at 400 °C min^{-1} under vacuum (1 Torr) was denoted as GN400V. The graphene films with less layer number are also referred to the thinner films (vice versa). Due to the conformal growth of graphene films on the Ni foam, these samples are considered to have nearly same surface area. The mass of graphene films for GN40, GN80, GN160, GN400 and GN400V are 1.9, 2.3, 2.6, 2.7 and 2.8 mg, respectively.

2.2. Characterization

Field-emission scanning electron microscope (SEM) pictures were taken using a FEI Quanta 600 FEG with an acceleration voltage of 5 kV. Raman spectroscopy measurements were conducted on a Horiba Aramis confocal microprobe Raman instrument with He–

Ne laser (λ = 632.8 nm) at ∼0.5 mW incident power. X-ray diffraction (XRD) was performed with Cu-Kα radiation (λ = 1.54056 Å) on a Bruker D8 X-ray diffractometer.

2.3. Electrochemical measurements

Electrochemical measurements, including cyclic voltammetry (CV, CHI 660D workstation), electrochemistry impedance spectra (Inphaze® impedance spectrometer) and galvanostatic charge/discharge curves (NEWARE BTS battery tester) were carried out in a three-electrode electrochemical cell using an Ag/AgCl (1 M KCl-filled) electrode as the reference electrode, a platinum wire as the counter electrode and the graphene/Ni-foam composite as the working electrode. The electrolyte was a mixture of 1 M NaAc + 1 M MgSO$_4$ aqueous solution, which can inhibit the corrosion of Ni foam [16]. The electrolyte was saturated with N$_2$ by bubbling with N$_2$ for 15 min prior to the start of each experiment. A flow of N$_2$ was maintained over the electrolyte during the measurements to ensure continuous N$_2$ saturation.

The specific capacitances were calculated for CV by integrating the area of the profiles based on the following equation:

$$C = \int_{E_1}^{E_2} i(E)\mathrm{d}E/(2(E_2 - E_1)m\nu) \tag{1}$$

where C is the specific capacitance, $\int_{E_1}^{E_2} i(E)\mathrm{d}E$ is the total voltammetric charge obtained by integration of the positive and negative sweep in cyclic voltammograms, $(E_2 - E_1)$ is the potential window width, m is the mass of the graphene films, and ν is the potential scan rate. The capacitance of graphene films was obtained by subtracting the contribution of the nickel substrate (0.2 F g^{-1}) from the total capacitance of graphene/Ni-foam composites. Impedance spectroscopy measurements were performed at a bias potential of 0 V with a sinusoidal signal of 5 mV over a frequency range from 100 kHz to 0.1 Hz. The charge/discharge current density was 0.25 A g^{-1} in the voltage range between −0.45 and 0.55 V. The specific capacitance, as determined from galvanostatic charge/discharge curves, was calculated in accordance with the following equation:

$$C = I \times t/(\Delta V \times m) \tag{2}$$

where C is the specific capacitance of the samples, I is the current during discharge process, t is the discharge time, ΔV is the potential window, and m is the mass of the graphene films.

3. Results and discussion

The formation of graphene on a nickel substrate involves carbon dissolving/segregating processes [17]. It has been reported that the cooling rate affects the amount of segregated carbon and the number of layers of graphene, i.e., thinner graphene forms at relatively slow rates [18,19]. SEM observation shows all nickel substrates are wrapped by graphene films after the CVD process, indicating highly efficient growth. At certain edges of the Ni foam struts, the graphene films can be observed. Fig. 1(a) shows that the extruded films on GN40 are transparent, exhibiting the characteristics of ultrathin films. The films on GN400V possess straight ridges and opaque surface due to the thicker film structure (Fig. 1(b)). It implies that GN400V has more layers of graphene relative to GN40. Fig. 2 displays the representative as-grown graphene on the struts of Ni foam. The polygonal cracks on the blank Ni foam are intergranular on the strut surface, and the grain
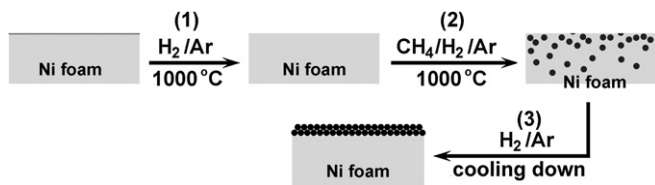
Scheme 1. Schematic diagram of the synthesis of graphene films on Ni foam. (1) Removing surface oxide layer of Ni foam. (2) Carbon dissolving process. (3) Carbon segregating to form graphene films.
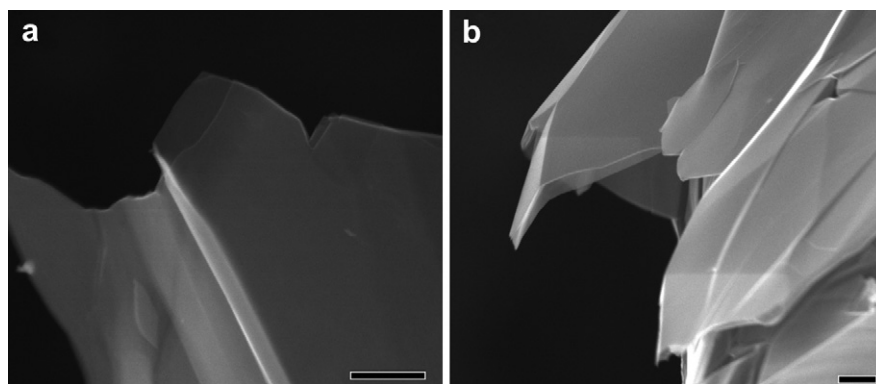
Fig. 1. SEM images of as-grown graphene films on the edge of Ni foam, (a) GN40 and (b) GN400V. Scale bar, 500 nm.
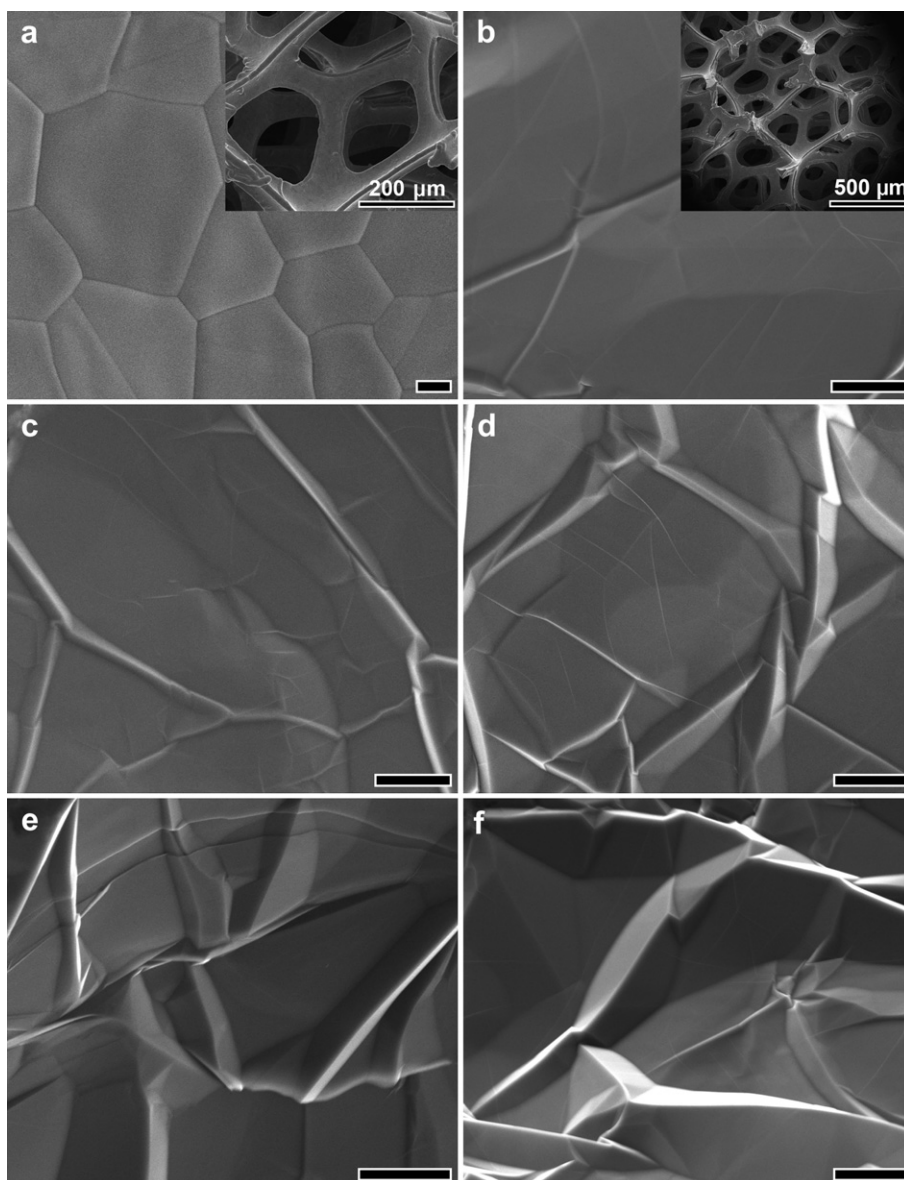

Fig. 2. SEM images of the as-grown graphene films on the struts of Ni foam, (a) blank Ni foam before CVD growth showing cracks with straight and clear grain boundaries. (b) GN40, (c) GN80, (d) GN160, (e) GN400 and (f) GN400V. Scale bar, 2 μm. The insets with low magnification show the three-dimensional structure configurations.

boundaries are straight and legible (Fig. 2(a)). After the CVD process, graphene layers with different wrinkles are coated on the surface of Ni foam (Fig. 2(b)–(f)). The three-dimensional configuration of Ni foam was preserved in all cases due to the structure-directed template effect as shown in the inset of Fig. 2(b). However, the coarseness and wrinkle distribution are quite different for the different cooling rates. For the sample that was cooled at 40 °C min^{-1}, the graphene films, on a scale of more than a dozen of microns squared, are evenly attached on the nickel strut planes (Fig. 2(b)). The grain boundaries of nickel become blurred, and no obvious wrinkles can be observed. When the cooling rate increased to 80 °C min^{-1}, wrinkles form on the surface due to large amounts of carbon separated from the nickel substrate (Fig. 2(c)). As the cooling rate (160 and 400 °C min^{-1}) further increases, the wrinkles distort stepwise to a larger degree (Fig. 2(d), (e)). The graphene layers reportedly will absorb the strain energy to form wrinkles by mechanical deformation at defect lines [20]. Under rapid cooling conditions, abundant dissolved carbon segregates and tends to bunch and overlap to lower the film's surface energy, which results in an increased number of wrinkles on thicker graphene films. In addition, GN400V displays the most distorted wrinkles (Fig. 2(f)), implying that vacuum can promote the segregation of dissolved carbon from the Ni foam [21].

Fig. 3 shows the typical Raman spectra of the graphene films derived from the CVD process at different cooling rates. The spectra consist of two Raman bands centered at 1582 and ∼2670 cm^{-1}, which correspond to the characteristic G and 2D modes of graphene, respectively [22]. The G peak is ascribed to the symmetry-allowed graphite band, and the 2D peak corresponds to the second-order zone-boundary phonons. No disorder-induced D band (around 1350 cm^{-1}) is observed in any graphene films, indicating the high quality of graphene on Ni foam substrate. According to the shape and position of the 2D band as well as the 2D to G peak intensity ratio (I_{2D}/I_G), the layer number of graphene films can be distinguished [20]. It can be seen that the peak position of the 2D band is apparently up-shifted and broadened with the increasing cooling rate. The ratio of I_{2D}/I_G for the sample GN40 is 0.71, which approximates to three layers [20–22]. From GN40 to GN400 the I_{2D}/I_G ratio decreases gradually, indicating that the layer number of graphene increases when increasing the cooling rate. For the sample GN400V, the I_{2D}/I_G decreases to 0.25, lower than that of GN400 (0.28), showing the further increase in layer number. This indicates that the application of vacuum as an outward drawing force helps to accelerate the carbon segregation from the Ni foam, resulting in the formation of thicker graphene films [21].

XRD patterns of graphene films show the characteristic peak [002] of the graphite phase in the range of 22–31° (Fig. 4). The peaks of the samples are up-shifted gradually with the increasing cooling rate. The [002] peak of GN40 is found at $2\theta = 26.38°$, while for GN80, GN160, GN400 and GN400V, the peak shifts to 26.43°, 26.49°, 26.57° and 26.63°, respectively. Note that the peak position of GN400V is close to that of the graphite (26.62°). According to Bragg's law ($n\lambda = 2d\sin\theta$), calculation of the graphene interlayer spacing reveals that the d_{002} spacing of the graphene films decreases as the cooling rate is increased. GN40 possesses the widest d_{002} spacing (3.376 Å), while the spacing of GN400V (3.345 Å) is more commensurate with crystal graphite (3.348 Å). These results are consistent with those reported by Soin et al. [23]. The variance of the [002] plane spacing is attributed to the different interactions between the nickel substrate and graphene films, which depend on the layer number of graphene. With the layer number increasing, the influence of the nickel substrate on the graphene films decreases gradually, leading to nearly the same spacing of GN400V to that of graphite. In addition, the appearance of more wrinkles on the multi-layer graphene (Fig. 2(c)–(f)) supports the weaker interaction between the thicker graphene films and the nickel substrate.

The supercapacitive properties of graphene films were investigated using CV, electrochemical impedance and galvanostatic charge/discharge testing. Ni foam, previously used as catalyst for producing graphene, acted directly as the current collector for these composites. The transfer procedure of graphene to another target substrate was circumvented; therefore, the capacitive behavior of as-grown graphene on Ni foam can be studied exclusively. Fig. 5(a) shows that the CV profiles of all graphene films exhibit nearly rectangular shapes in the range of −0.45−0.55 V at 5 mV s^{-1}, which is a typical double-layer capacitive behavior. In addition, the current density increases linearly with the scan rate, and the linear
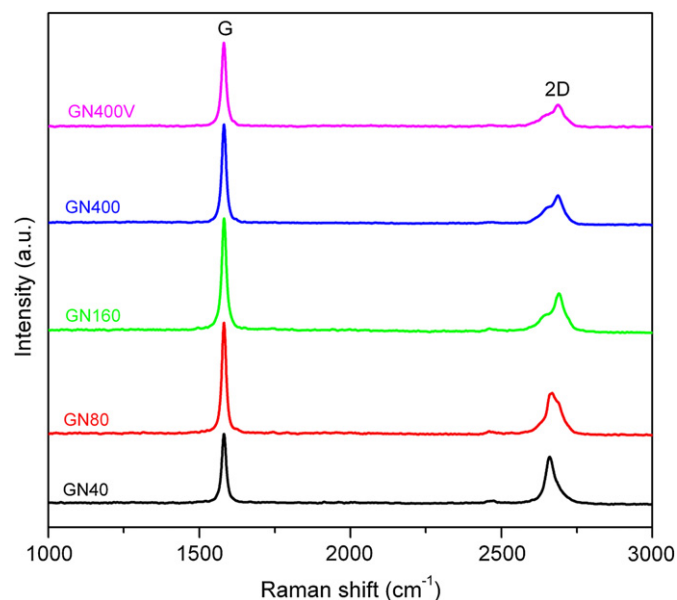

Fig. 3. Raman spectra of the samples grown at various cooling rates with an excitation wavelength of 632.8 nm. The I_{2D}/I_G ratios for GN40, GN80, GN160, GN400 and GN400V are 0.71, 0.36, 0.32, 0.28 and 0.25, respectively.
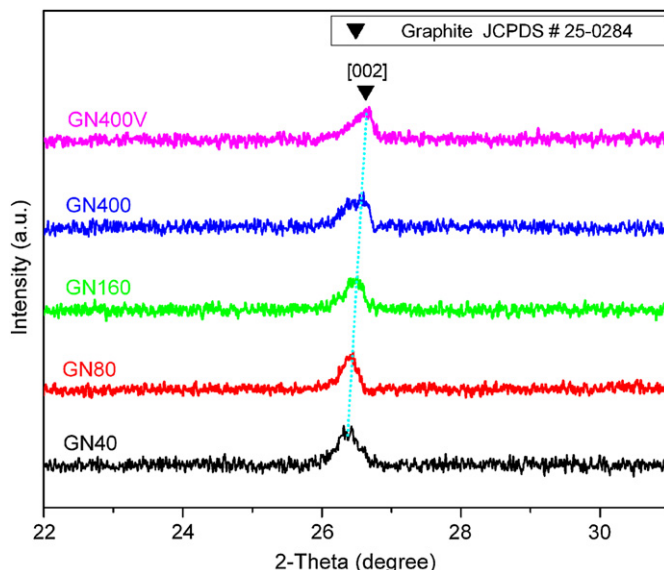

Fig. 4. XRD patterns of graphene films grown at different cooling rates.
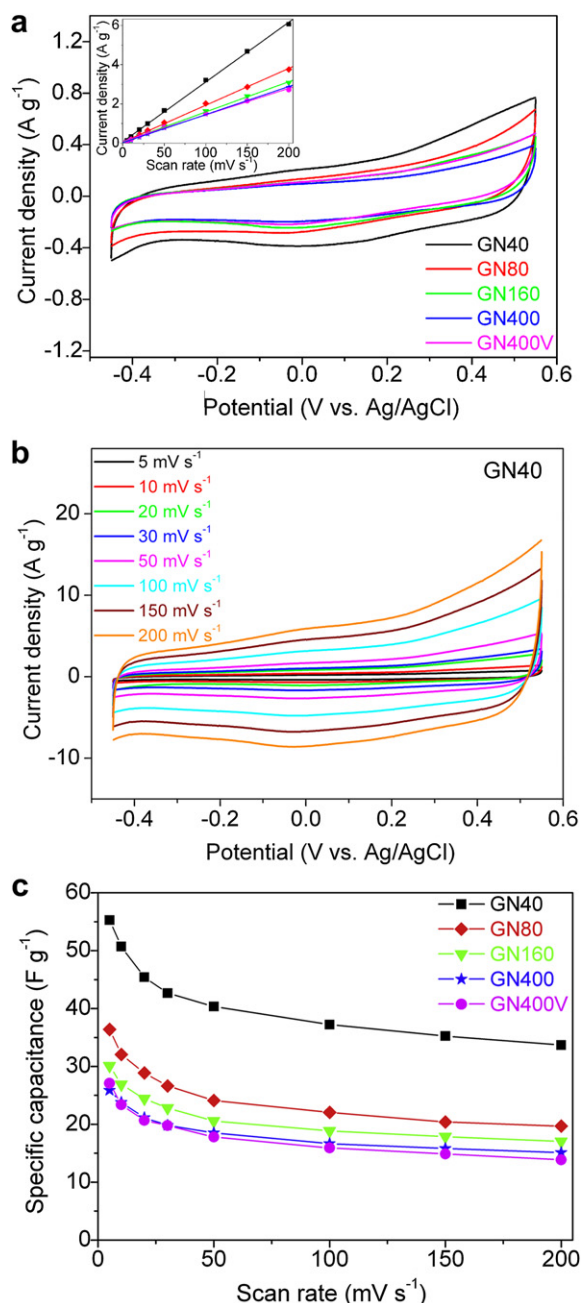
Fig. 5. (a) CV curves of graphene films at a scan rate of 5 mV s^{-1} in 1 M NaAc + 1 M MgSO$_4$ solution. The inset shows the dependence of the current density obtained at 0.05 V from the anodic branch of the composites upon the CV scan rates. (b) CV curves of GN40 at various scan rates from 5 to 200 mV s^{-1} in 1 M NaAc + 1 M MgSO$_4$ solution. (c) Plots of specific capacitance change with scan rate for graphene films.

walled carbon nanotubes [24]. The profile of the CV curves of GN40 still remains rectangular at a high scan rate of 200 mV s^{-1} (Fig. 5(b)), confirming its good capacitive behavior. With increasing scan rate, the specific capacitances of all graphene films decrease gradually and GN40 possesses much higher specific capacitance compared to other films (Fig. 5(c)). This finding can be attributed to the easy electron transport from graphene to the substrate in GN40 resulted from the stronger interaction of graphene films with the substrate. Moreover, the relatively higher mass–area ratio of GN40 renders it a better capacitive behavior.

The impedance spectra of the graphene films were analyzed firstly using Nyquist plots, which show the imaginary component ($-Z''$) of the impedance against the real component (Z'), as shown in Fig. 6(a). Each data point is at a different frequency with the lower left portion of the plot corresponding to higher frequencies. The intercept of the plot on the Z' axis represents the magnitude of the solution resistance (R_s) of the system, which determines the rate that the films can be charged/discharged. The value of R_s for all films is low, in the range of 0.75–0.95 Ω, indicating the graphene films have excellent power capabilities [26]. All the impedance spectra of the films consist of an inconspicuous arc in the higher frequency region and a straight line in the lower frequency region.
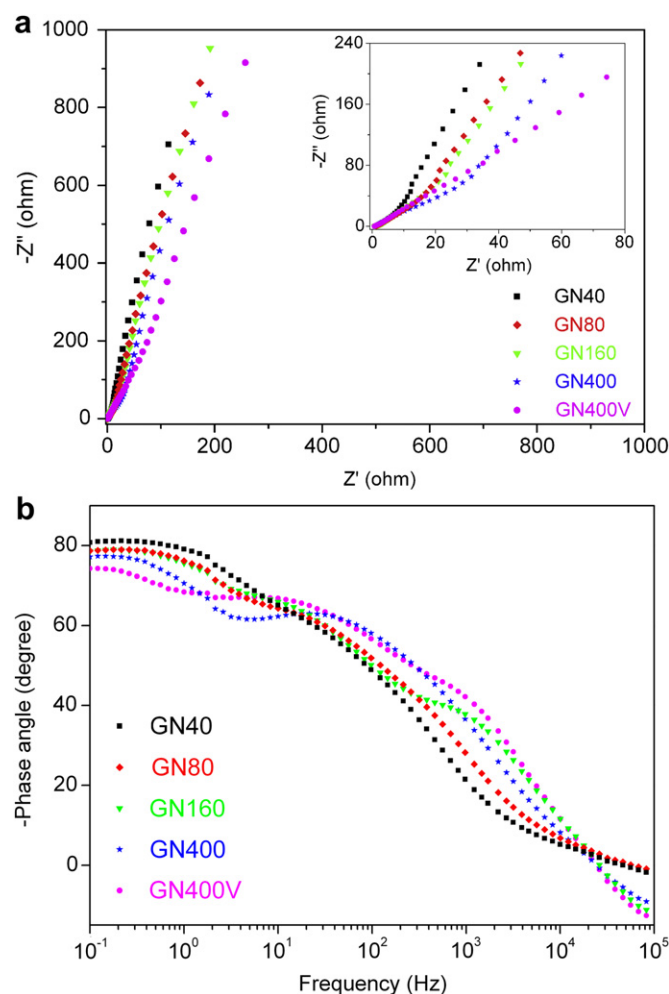

Fig. 6. Electrochemical impedance spectra of graphene films on the nickel substrate in 1 M NaAc + 1 M MgSO$_4$ solution. (a) Nyquist plots: Z' represents real impedance and Z'' represents the imaginary impedance. The inset shows the magnified high-frequency region. (b) Corresponding Bode phase plots with phase angle as a function of logarithmic frequency.

correlation coefficient is more than 0.998 for all graphene films (the inset in Fig. 5(a)) implying that the graphene on the nickel substrate possesses excellent power characteristics. The specific capacitances of GN40, GN80, GN160, GN400 and GN400V at 5 mV s^{-1} are calculated as 55.3, 36.4, 30.1, 25.9 and 27.1 F g^{-1}, respectively. Notably, the specific capacitance of GN40 is nearly two times that of other films. As recently reported, various nanostructured carbons have been tested for double-layer capacitor applications, such as single- and multi-walled carbon nanotubes, which have specific capacitance of 64 and 14 F g^{-1}, respectively [24,25]. GN40 has comparable specific capacitance with the capacitor based on single-

The high-frequency arcs are related to the interfacial charge-transfer resistance (R_c) between the graphene film and the nickel substrate. The inconspicuous arcs indicate a low R_c in the films making them promising as electrode materials for supercapacitors [10]. GN40 has the shortest arc in the high-frequency region, indicating the smallest charge-transfer resistance (inset in Fig. 6(a)). As the layer number of graphene films increases, the R_c of GN80, GN160, GN400 and GN400V increases to some extent. Moreover, GN40 shows the most vertical line in the lower frequency region, suggesting that it has the best capacitive behavior compared to other films [10,12]. These results were also supported by the Bode diagram with phase angle as a function of logarithmic frequency, as shown in Fig. 6(b). At lower frequencies (0.1–2 Hz), the phase angle of GN40 shows a plateau at the highest angle (more close to 90° compared to others), indicating a typical capacitive characteristic [27,28]. GN80 and GN160 have similar plateaus at lower angles. As for the samples GN400 and GN400V, the plateau becomes shorter and the angle decreases further more, which is a result of the deviation from ideal capacitor. In the medium frequency range, GN40 has a very broad and weak band from 2 to 9×10^3 Hz, implying the smallest charge-transfer resistance [29,30]. The curve of GN80 has a similar characteristic as that of GN40. With increasing thickness and wrinkles, the bands for GN160, GN400 and GN400V become intense and shift to high frequencies, which might be caused by the complex charge-transfer processes.

The cyclability properties of the graphene films were investigated by galvanostatic charge/discharge testing. The insets in Fig. 7 show that both charge and discharge curves of GN40 and GN400V are nearly linear and symmetrical, which supports that the graphene films have typical capacitive properties. The films displayed excellent cyclability during cycling tests up to 1000 cycles, showing potential prospects as the electrode materials of electric double-layer capacitors. This may profit from the preferable three-dimensional structures of the composites, in which electrolyte ions can penetrate and diffuse easily during the charge/discharge cycles. The specific capacitance of GN40 is 63.7 F g^{-1} at the 1000th cycle, nearly two times that of other graphene films. It confirms that GN40 with thin and even layers shows superior capacitive properties.
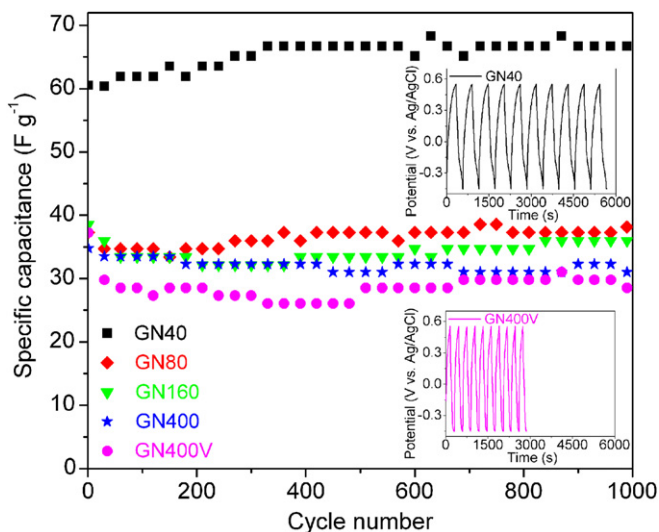
4. Conclusion

We have successfully synthesized graphene films with different numbers of layers by varying the cooling rate during the CVD process. It was found that the electrochemical properties of the graphene films depended on the number of layers. The graphene films with three layers show low charge-transfer resistance and higher specific capacitance than those of thicker graphene films. This result is likely due to the stronger interaction between the thinner graphene films and the nickel substrate. This study provides a valuable method for developing highly active graphene-based materials for electrochemical energy storage with the advantages of both high capacitance and excellent power capabilities.

Fig. 7. Charge/discharge cyclability of graphene films on the nickel substrate from the 1st to the 1000th cycle. The galvanostatic results were obtained at a charge/discharge current density of 0.25 A g^{-1} in the 1 M NaAc + 1 M MgSO$_4$ solution. The insets show the chronopotentiograms from the 1st to 10th cycle for the samples GN40 and GN400V.

References

[1] K.S. Novoselov, A.K. Geim, S.V. Morozov, D. Jiang, Y. Zhang, S.V. Dubonos, I.V. Grigorieva, A.A. Firsov, Science 306 (2004) 666–669.
[2] A.K. Geim, Science 324 (2009) 1530–1534.
[3] A.K. Geim, K.S. Novoselov, Nat. Mater. 6 (2007) 183–191.
[4] Y. Liang, Y. Li, H. Wang, J. Zhou, J. Wang, T. Regier, H. Dai, Nat. Mater. 10 (2011) 780–786.
[5] X.Y. Peng, X.X. Liu, D. Diamond, K.T. Lau, Carbon 49 (2011) 3488–3496.
[6] Y. Wu, Y.M. Lin, A.A. Bol, K.A. Jenkins, F. Xia, D.B. Farmer, Y. Zhu, P. Avouris, Nature 472 (2011) 74–78.
[7] X. Li, W. Cai, J. An, S. Kim, J. Nah, D. Yang, R. Piner, A. Velamakanni, I. Jung, E. Tutuc, S.K. Banerjee, L. Colombo, R.S. Ruoff, Science 324 (2009) 1312–1314.
[8] Z. Chen, W. Ren, B. Liu, L. Gao, S. Pei, Z. Wu, J. Zhao, H. Cheng, Carbon 48 (2010) 3543–3550.
[9] L. Zhao, K.T. Rim, H. Zhou, R. He, T.F. Heinz, A. Pinczuk, G.W. Flynn, A.N. Pasupathy, Solid State Commun. 151 (2011) 509–513.
[10] M.D. Stoller, S. Park, Y. Zhu, J. An, R.S. Ruoff, Nano Lett. 8 (2008) 3498–3502.
[11] J.R. Miller, R.A. Outlaw, B.C. Holloway, Science 329 (2010) 1637–1639.
[12] Y. Wang, Z. Shi, Y. Huang, Y. Ma, C. Wang, M. Chen, Y. Chen, J. Phys. Chem. C 113 (2009) 13103–13107.
[13] W. Zhu, C. Dimitrakopoulos, M. Freitag, P. Avouris, IEEE Trans. Nanotechnol. 10 (2011) 1196–1201.
[14] Z. Luo, T. Yu, K. Kim, Z. Ni, Y. You, S. Lim, Z. Shen, S. Wang, J. Lin, ACS Nano 3 (2009) 1781–1788.
[15] Z. Chen, W. Ren, L. Gao, B. Liu, S. Pei, H. Cheng, Nat. Mater. 10 (2011) 424–428.
[16] Y. Wang, A. Yuan, X. Wang, J. Solid State Electrochem. 12 (2008) 1101–1107.
[17] H.J. Park, J. Meyer, S. Roth, V. Skakalova, Carbon 48 (2010) 1088–1094.
[18] Q. Yu, J. Lian, S. Siriponglert, H. Li, Y.P. Chen, S.S. Pei, Appl. Phys. Lett. 93 (2008) 113103.
[19] A. Reina, S. Thiele, X. Jia, S. Bhaviripudi, M.S. Dresselhaus, J.A. Schaefer, J. Kong, Nano Res. 2 (2009) 509–516.
[20] S.J. Chae, F. Gunes, K.K. Kim, E.S. Kim, G.H. Han, S.M. Kim, H. Shin, S. Yoon, J. Choi, M.H. Park, C.W. Yang, D. Pribat, Y.H. Lee, Adv. Mater. 21 (2009) 2328–2333.
[21] X. Liu, L. Fu, N. Liu, T. Gao, Y. Zhang, L. Liao, Z. Liu, J. Phys. Chem. C 115 (2011) 11976–11982.
[22] A.C. Ferrari, J.C. Meyer, V. Scardaci, C. Casiraghi, M. Lazzeri, F. Mauri, S. Piscanec, D. Jiang, K.S. Novoselov, S. Roth, A.K. Geim, Phys. Rev. Lett. 97 (2006) 187401.
[23] N. Soin, S.S. Roy, C. O'Kane, J.A.D. McLaughlin, T.H. Lim, C.J.D. Hetherington, CrystEngComm 13 (2011) 312–318.
[24] S.R.C. Vivekchand, C.S. Rout, K.S. Subrahmanyam, A. Govindaraj, C.N.R. Rao, J. Chem. Sci. 120 (2008) 9–13.
[25] P. Simon, Y. gogotsi, Nat. Mater. 7 (2008) 845–854.
[26] C.W. Huang, C.M. Chuang, J.M. Ting, H. Teng, J. Power Sources 183 (2008) 406–410.
[27] S.H. Aboutalebi, A.T. Chidembo, M. Salari, K. Konstantinov, D. Wexler, H.K. Liu, S.X. Dou, Energy Environ. Sci. 4 (2011) 1855–1865.
[28] X. Xie, L. Gao, Carbon 45 (2007) 2365–2373.
[29] N. Yang, J. Zhai, D. Wang, Y. Chen, L. Jiang, ACS Nano 4 (2010) 887–894.
[30] K.M. Lee, C.W. Hu, H.W. Chen, K.C. Ho, Sol. Energy Mater. Sol. Cells 92 (2008) 1628–1633.